

Lab on a Chip

Accepted Manuscript



This is an *Accepted Manuscript*, which has been through the Royal Society of Chemistry peer review process and has been accepted for publication.

Accepted Manuscripts are published online shortly after acceptance, before technical editing, formatting and proof reading. Using this free service, authors can make their results available to the community, in citable form, before we publish the edited article. We will replace this *Accepted Manuscript* with the edited and formatted *Advance Article* as soon as it is available.

You can find more information about *Accepted Manuscripts* in the [Information for Authors](#).

Please note that technical editing may introduce minor changes to the text and/or graphics, which may alter content. The journal's standard [Terms & Conditions](#) and the [Ethical guidelines](#) still apply. In no event shall the Royal Society of Chemistry be held responsible for any errors or omissions in this *Accepted Manuscript* or any consequences arising from the use of any information it contains.

ARTICLE

Micro Propulsion by Acoustic Bubble for Navigating Microfluidic Spaces

Cite this: DOI: 10.1039/x0xx00000x

Jian Feng^a, Junqi Yuan^b and Sung Kwon Cho^c,

Received 00th January 2012,
Accepted 00th January 2012

DOI: 10.1039/x0xx00000x

www.rsc.org/

This paper describes an underwater micro propulsion principle where a gaseous bubble trapped in a suspended microchannel and oscillated by an external acoustic excitation generates a propelling force. The propelling swimmer is designed and microfabricated out of parylene in micro scale (equivalent diameter of the cylindrical bubble is around 60 μm) using microphotolithography. The propelling mechanism is studied and verified by computational fluid dynamics (CFD) simulations as well as experiments. The acoustically excited and thus periodically oscillating bubble generates alternating flows of intake and discharge through an opening of the microchannel. As the Reynolds number of oscillating flow increases, the difference between intake and discharge flows becomes significant enough to generate a net flow (microstreaming flow) and a propulsion force against the channel. As the size of device is reduced, however, the Reynolds number is also reduced. To maintain the Reynolds number in a certain range and thus generate a strong propulsion force in the fabricated device, the oscillation amplitude of bubble is maximized (resonated) and the oscillation frequency is set high (over 10 kHz). Propelling motions by a single bubble as well as an array of bubbles are achieved in microscale. In addition, the micro swimmer demonstrates payload carrying. This propulsion mechanism may be applied to microswimmers that navigate microfluidic environments and possibly narrow passages in human bodies to perform bio sensing, drug delivery, imaging, and microsurgery.

Introduction

There have been a large number of research attempts to develop microswimmers to navigate passages in microfluidic devices and even narrow spaces inside human bodies to perform drug delivery, micro surgery, bio sensing, imaging, etc.¹⁻⁴. A variety of physical principles have been adopted to generate propulsion forces for the microswimmers. For example, artificial micro flagella based on bacteria propulsion were built that could produce corkscrew motions in six degrees of freedom under an external magnetic field⁵⁻⁷. Dreyfus *et al.* developed a similar artificial flagellum but based on flexible oar motions⁸ that were also generated by an external magnetic field. The above magnetic actuations usually need a bulky, complex external system with linear and rotational traversing mechanisms to generate strong magnetic fields⁷. Thrusts by natural microorganisms^{9, 10} were also harnessed for microswimmers, although they mainly suffer from difficulties in commanding and controlling. In addition, a large number of research activities were focused on propulsion by chemical reactions (especially catalytic reactions)¹¹⁻¹⁷. Some of them demonstrated attaching, carrying and releasing of cargos. However, propulsion based on chemical/biological reactions has issues in continuous supplying of chemical/biological fuels

and their compatibility with microfluidic or *in vivo* environments^{13, 14}. Currently, it is of paramount importance to develop micro propulsion that has a simple structure, is wirelessly powered and controlled, and efficiently works in the general microfluidic as well as *in vivo* fluids.

The common in macroscale yet interesting propulsion in microscale is to exhaust high-speed fluid through a nozzle. One of the well-known early attempts is the putt-putt boat propulsion, which was powered by a simple heat engine along with a boiler and one or two steam exhaust tubes that converted water into steam periodically¹⁸. Recently, Dijkink *et al.*¹⁹ built an acoustic bubble propulsion device using the conventional macroscale fabrication method, which is called 'acoustic scallop'. A gaseous bubble in the device periodically oscillates under acoustic excitation. The device is 750 μm in diameter and 2-4 mm in length. The bubble oscillation generates a quasi-steady streaming flow that eventually produces propulsion forces on the device. This device could swim at maximum 1.35 mm/s uni-directionally. Besides acoustic excitation, AC-electrowetting²⁰ and thermal excitations²¹ were made to oscillate bubbles. The obvious excellence of acoustic excitation is to transmit power (acoustic field) wirelessly using a simple external acoustic actuator, which has motivated to widen its

application to many microfluidic components²² such as pumps^{23, 24}, mixers^{22, 23}, manipulators²⁵⁻²⁸, etc.

Although the above acoustic scallop is impressive and interesting, any smaller device would be more useful and applicable for many microfluidic dimensions or *in vivo* biological and medical propulsion applications. In order to navigate typical microfluidic devices and narrow passages (e.g., arterioles and venules) in the body, the bubble diameter should be reduced down to at most tens μm or even smaller. The critical dimension to navigate narrow and serpentine passages is the diameter of cylindrical bubble. Here, one may question whether or not the acoustic bubble propulsion is still effective for even smaller swimmers (bubbles) where the viscous effect is more dominant and thus the streaming flow might be possibly vanished.

In this paper, we study this question numerically and experimentally by using computational fluid dynamics (CFD) simulations and examining microfabricated devices. We use the microfabrication (micro photolithographic) technology to make microswimmers whose equivalent diameter of bubble (microchannel) is as small as $60\ \mu\text{m}$. As opposed to the conventional fabrication, the micro fabrication method lends itself to high flexibility and easiness for precise control of the dimensions, shape and arrangement of single bubble as well as multiple bubbles in microscale. The backbone of the device is two parylene layers such that the device is flexible, transparent, and biocompatible. By tuning the frequency of the external acoustic field to the resonance of the entire setup including the bubble, the bubble can strongly oscillate and generate a propulsion force. The maximum velocity of this device could reach over $40\ \text{mm/s}$ (about 80 body lengths per second). In addition, the device demonstrates payload carrying. All these operations are made wirelessly by a single external piezoelectric actuator, not requiring any complex spatial modulation of the acoustic field. The preliminary data of this work have been previously reported in the conference²⁹.

Working Principle and CFD (Computational Fluid Dynamics) Analysis

The working principle of the present device is based on the acoustic scallop. A gaseous bubble is trapped in a microchannel with one end section open (Fig. 1). When an acoustic field (pressure fluctuation) is applied to the bubble, the bubble meniscus at the opening of the microchannel periodically oscillates back and forth because the gas bubble is compressible. This oscillation creates periodical intake and discharge flows near the opening. One may expect that the entire flow field in the intake may be identical to that in the discharge except its direction is opposite. In this paper this case is called 'symmetric' flow. However, it is not necessarily true when the Reynolds number ($Re = \rho Ul/\mu$) becomes high. Here, U is the flow speed, ρ is the density of the fluid, l is the characteristic dimension (commonly bubble diameter) and μ is the dynamic viscosity of the fluid. Note that Re represents the ratio of inertia to viscous forces. If the flow fields are not

simply symmetric, the mean velocity field that is time-averaged over the period is not zero, which is called microstreaming flow. In this case, the magnitudes of total momentum flux and stresses on the device surface during the intake process would not be equal to those during the discharge process. Note that regardless of Re , the total mass flux through the channel during the intake process must be equal to that during the discharge process unless there is mass accumulation or loss inside of the channel. Consequently, the difference in the momentum flux and stresses generates a propelling force acting on the device.

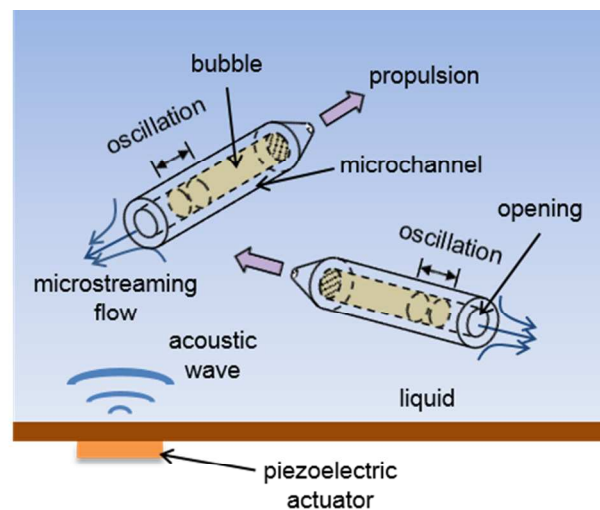


Fig. 1 Concept of propulsion by an oscillating bubble.

The difference in the momentum flux and stresses may be initiated and amplified by localized mechanisms (for example, the boundary layer separation that occurs in the viscous flow¹⁹). Jenkins³⁰ showed that even for the inviscid flow the asymmetric fluid patterns still exist. This asymmetric flow originates from the nonlinear (inertia) term in the Navier-Stokes equations, which is $\rho(\vec{V} \cdot \nabla)\vec{V}$ where \vec{V} is the flow velocity vector and ∇ is the del operator. This may be easily explained by replacing \vec{V} with $-\vec{V}$ in the Navier-Stokes equation. Due to the nonlinear (product) term, the replaced Navier-Stokes equation is not identical with the original Navier-Stokes equation. This means that suppose \vec{V} is a solution of the Navier-Stokes equation, $-\vec{V}$ may not be necessarily a solution of the Navier-Stokes equation. As far as this nonlinear term comes into play, the flow fields around the channel cannot be simply reversed but would be different between intake and discharge. That is, the asymmetric flow patterns should occur and leads to generation of the propulsion force.

As the propulsion device becomes small, so do the Reynolds number and thus the effect of the nonlinear (inertia) term. In this case, the flow patterns during the intake and discharge processes become more symmetric, and thus the propulsion force becomes weaker. Eventually, when $Re = 0$, the flow would be perfectly symmetric³¹ and the propulsion force would be zero since the effect of the nonlinear (inertia)

term is vanished. Therefore, Re is a critical parameter to determine whether or not this propulsion works efficiently.

Here, one may question how small Re can be reduced yet generating a substantial propulsion force. During oscillation, the velocity is time-varying. Using the peak velocity ($= 2\pi fa$) where f is the oscillation frequency and a is the oscillation amplitude, the Reynolds number can be re-defined for the oscillatory flow,

$$Re = \frac{2\rho R(2\pi f)a}{\mu}, \quad (1)$$

where R is the radius of the microchannel. Although the device becomes small (i.e., R becomes small), it is possible to retain the Reynolds number to be a certain range - where propulsion is still effective - by increasing the frequency f and/or the amplitude a .

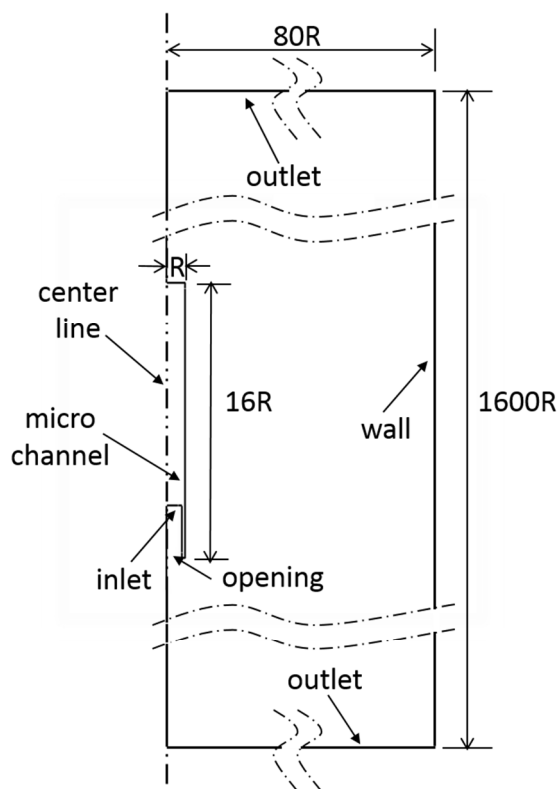


Fig. 2 Computational domain of the bubble propulsion device placed and centered between two walls. Only the right half of the full physical domain is simulated under the assumption of flow symmetry between the left and right halves.

To investigate the effect of Re on propulsion, 2-D CFD simulations were carried out for simplified flow conditions using the commercial CFD package of ANSYS Fluent[®]. The right half of physical domain is chosen for a computational domain, as shown in Fig. 2. Since the flow is assumed symmetric between the left and right halves of the full physical domain, only the flow in the right half is simulated using a symmetric condition along the centerline. A one-end open

channel - which holds a bubble - is centered between two walls. The width, length and wall thickness of the microchannel are $2R$, $16R$ and $0.04R$, respectively. The depth of the computational domain is set to be the unit length. The boundary conditions are that the upper and lower outlets of the domain are set to be 'outflow' and the no slip condition is applied to the solid walls. For the sake of simplicity, the bubble is not included in the simulation. Instead, the uniform velocity profiles are assigned at $3R$ on the inside from the edge of the opening (annotated as "inlet" in Fig. 2). Although the oscillatory flow in the device is transient, two steady-state cases of (i) intake and (ii) discharge with a constant flow rate through the microchannel are computed and compared for various Re . This substantially simplifies computation process yet allows us to understand the asymmetric behavior between intake and discharge. The number of the computational grids is about 180,000.

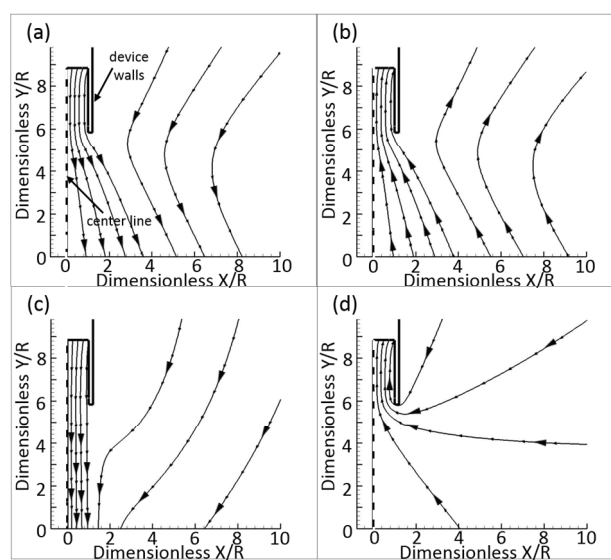


Fig. 3 Numerical results of streamlines for both discharge and intake flows at two Reynolds numbers (a) $Re = 0.38$, discharge, (b) $Re = 0.38$, intake, (c) $Re = 380$, discharge and (d) $Re = 380$, intake.

Fig. 3 shows streamlines for $Re = 0.38$ and $Re = 380$. The flow rates for intake and discharge cases are set equal. The stream function value has an equal increment between the adjacent streamlines. As shown in Figs. 3 (a) and (b) for $Re = 0.38$, the streamlines for both intake and discharge spread in a wide angle over the computational domain. Their distributions and patterns are almost the same for both cases. The difference is that the flow directions are opposite. That is, the flow is symmetric between intake and discharge. The magnitude difference in momentum and all the forces acting on the channel between the two cases would be nearly zero. That is, the net (propulsion) force would be almost zero if these two flows are alternated. On the contrary, when $Re = 380$, the difference between intake and discharge is clearly distinct as shown in Figs. 3 (c) and (d). For discharge, the streamlines starting from the opening of the microchannel extend straightly

in the axial direction of the channel. For intake, however, the streamlines that are almost evenly distributed in all direction are converged into the channel. The flow is even drawn from the backside of the channel opening. As a result, the propulsion force of the device should become substantial if the discharge and intake flows would be periodically alternated.

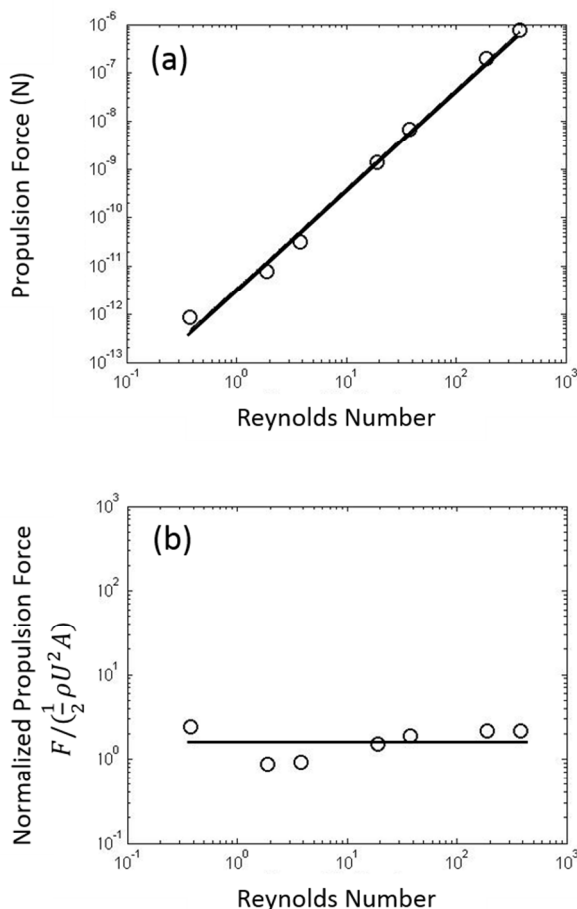


Fig. 4 Numerical Results of (a) propulsion forces and (b) normalized propulsion force at several Reynolds numbers.

The force acting on the channel (propulsion force) is calculated based on these 2-D numerical results at several Re numbers. A control volume for this calculation is defined identical to the outline (solid line) of the microchannel and its opening in Fig. 2. The pressure, viscous stresses and momentum flux are integrated and calculated over the entire control surfaces. The sum of these integrations of intake and discharge cases would indicate the propulsion force generated when the intake and discharge flows alternate. Fig. 4 (a) shows that the propulsion force monotonically increases as Re increases. This is consistent with the streamline patterns in Fig. 3 that the flow at large Re becomes more asymmetric between intake and discharge. Fig. 4 (b) shows the same data but the propulsion force is normalized by the momentum flux ($= \rho U^2 A/2$) through the channel inlet, where A is the cross-

sectional area of the channel opening and F is the propulsion force. Over the entire range of simulated Re , the normalized propulsion force stays nearly constant and could be curve-fitted from Fig. 4(b) as,

$$F \cong 0.8\rho AU^2 = 0.8\rho A(af)^2. \quad (2)$$

Here, the standard deviation for the coefficient 0.8 is 0.29. This simplest curve-fit makes it much easier to directly see the effects of the associated parameters, although it slightly compromises the accuracy compared to higher-order curve-fittings. Equation (2) reveals that the propulsion force is proportional to the momentum flux through the channel opening: the oscillating velocity at the channel opening is a key factor to generate strong propulsion in given channel dimensions. Note that the magnitude of the oscillating velocity is the product of oscillating frequency and amplitude. That is, *maintaining the oscillating frequency high and maximizing the oscillating amplitude is crucially important to generate substantially strong propulsion forces.*

For given device dimensions, the oscillating amplitude is maximized when the bubble oscillation is resonated. The spring-mass model¹⁹ predicted an expression on the resonant frequency (f_0):

$$f_0 = \frac{1}{2\pi} \sqrt{\frac{\kappa P_0}{\rho L_0 L_B}}, \quad (3)$$

where P_0 is the pressure of the undisturbed bubble, ρ the water density, L_0 the length of water column between the bubble interface and the channel outlet, L_B the length of the bubble, and $1 \leq \kappa \leq \gamma$ where γ is the ratio of specific heats of gas in the bubble. Here κ is determined to be 1.2 for the present case based on Chen and Prosperetti³². Note that equation (3) has no correction for the end effect²⁹. It was shown that equation (3) is in good agreement with the experiments¹⁹. In the present study, however, it turns out that predicting the resonance frequency is not easy, highly influenced by experimental set-up including the materials, dimensions and configuration of testing water tank. Therefore, we decide to directly measure the acoustic (oscillating) behavior of the entire system set-up and bubble.

Device Fabrication and Experimental Set-up

Testing devices are microfabricated using micro photolithography. In selecting the device material, the following requirements need to be taken into account. First, the channel surface has to be hydrophobic in order to hold a bubble inside the channel. In this case, the bubble can be automatically and easily trapped by simply submerging the channel into water. The bubble dimensions are defined by the channel dimensions. Second, the material should be transparent such that the bubble motion is observable during oscillation. In addition, it allows us to visualize the flow around the bubble interface by tracking seeded microparticles. Third, the density

of the material should be neither too high nor too low such that the overall density including the bubble is close to the water density. This ensures that the device would not float or sink and that the friction force with the water tank surface would be minimized. Fourth, the material has to be biocompatible³³. Last, it is preferable that the material is flexible. This would facilitate navigation of serpentine passages. Parylene meets the above requirements. In addition, since parylene is deposited by the chemical vapor deposition (CVD) process, the deposition is highly conformal with accurate thickness control.

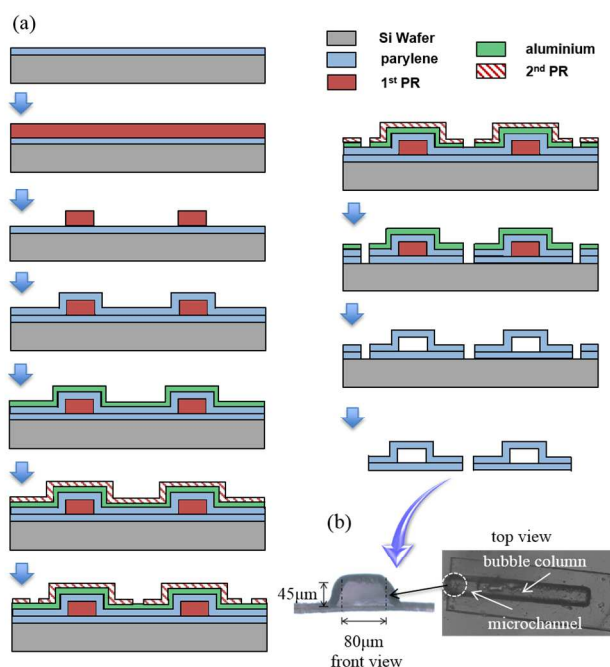


Fig. 5 (a) Fabrication of one-end open microchannel and (b) photo of fabricated device (top view and frontal view at the channel opening). The microchannel traps and holds an air bubble column. The end of the channel is opened by RIE etching.

The detailed microfabrication flow is shown in Fig. 5(a). It begins with the parylene coating process. A 7- μm thick parylene layer is coated on a silicon wafer by the CVD process, which serves as the bottom wall of the microchannel. The thickness of the microchannel should be carefully chosen. If it is too thick, the device becomes heavy enough to sink, contact the bottom wall of testing chamber, and increase friction with the wall. On the contrary, if the thickness is too small, the strength of the microchannel is reduced, which allows the channel itself to expand and shrink when the bubble is oscillated by the applied acoustic field. This would eventually reduce the oscillation amplitude of the bubble at the channel opening and thus propulsion force. It turns out that the 7- μm thickness is suitable for not confronting the above issues. The next step is to deposit a 45- μm photoresist (AZP 4620) layer on the parylene layer. This layer is patterned for a sacrificial layer to define the microchannel. Then, another 7- μm parylene layer is deposited on the sacrificial layer to form the upper wall and

sidewalls of the microchannels. Next, an aluminium layer is coated and patterned by wet etching using a masking of the second 2- μm photoresist layer (AZP 4210). The aluminium layer can be simultaneously etched by an alkaline-based photoresist developer when the second photoresist layer is developed. This aluminium layer is used for masking when one end of the microchannel is opened and the device is diced by the reactive ion etching (RIE) process. After the RIE process, all aluminium residues are removed by the alkaline-based photoresist developer. Finally, the sacrificial photoresist layer is completely removed by an acetone solution and the channel is released from the substrate. The front and top views of the fabricated microchannel are shown in Fig. 5 (b). When the device is diced by RIE, a sufficient margin is deliberately given such that the channel has a flap around it. This is only for the purpose of easy handling in device testing. Whenever needed, the flap can be easily removed by changing the mask design. The dimensions of the channel (bubble) are determined based on the CFD analysis and equation (3) such that the bubble resonates at high frequency to maintain $Re \sim 380$ and generate substantial propulsion forces. All the microchannels fabricated have the same height of 45 μm and width of 80 μm . The equivalent diameter of the present micro channel is 60 μm .

For acoustic actuation, a focused transducer may be used, whose acoustic output does not highly rely on the acoustic properties of the surrounding system. However, as the swimming device moves, the focused transducer may require a complex control system to trace the swimming device and to steer the acoustic output. To simplify the overall system setup, the acoustic field is generated by a non-focused disk-type piezoelectric actuator (27 mm in diameter and resonated at 4.6 \pm 0.5 kHz) glued to the sidewall of the water tank. The input signal is generated by a function generator and amplified by an amplifier. The signal to the actuator is monitored by an oscilloscope. The testing water tank is in the size of 11 \times 11 \times 5 cm^3 made of acrylic plates (3 mm thick). The experimental images are obtained by an inverted microscope connected to a high-speed camera (Phantom V7.3, Vision Research, Inc.). All images are bottom views through the acrylic bottom plate in the tank. A Laser Doppler Vibrometer (LDV, Micro System Analyzer Model MSA-400, Polytec, Inc.) is used to measure the oscillating velocity of the tank bottom plate at the position over which the device is tested. A miniature reference hydrophone (TC 4013, Teledyne RESON) is used to measure the amplitude of acoustic field generated by the piezoelectric actuator. The hydrophone is held vertically and its tip is kept 1 mm away from the water tank bottom. The acoustic pressures are measured at the center and four corners of the water tank and averaged.

Experimental Results

A device with 530 μm long micro channels is examined in the testing tank of 3 cm water level. When the device is submerged into water, an air bubble is automatically trapped inside of each microchannel. The bubble length is about 470 μm . The

remaining section (about 60 μm) of the channel is filled with water. The acoustic field is applied sweeping its frequency from 1 kHz to 14 kHz with an equal increment of 0.1 kHz. Equation (3) predicts the resonance frequency for the present bubble configuration to be 10.5 kHz while it is experimentally measured that the bubble oscillation is maximum at 11.2 kHz. The reason for discrepancy is discussed later in this section.

To see whether the streaming flow is generated near the opening of the channel, flow visualization is first performed by seeding 2- μm -diameter microparticle tracers in water. The device with an array of multiple microchannels is anchored to the bottom of the tank (Fig. 6, see the supplementary video clip 1, 3x slower). When the piezoelectric actuator is turned on, the bubble meniscus is oscillated back and forth periodically. Due to the motion of meniscus, the microparticles are also moving in the oscillating fluid. From high-speed camera images, it is found that oscillations of the microparticles and meniscus are exactly synchronized with the driving frequency, which confirms that the acoustic energy is the source for the fluid motion.

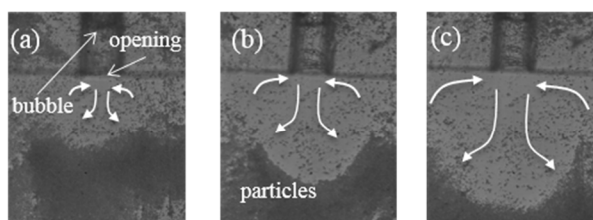


Fig. 6 Generation of streaming flow. After 1 minute bubble oscillation, seeding particles are pushed away from the channel opening, as the empty region is distinctively seen. Applied voltages to the piezoelectric actuator are (a) 77 (b) 126 and (c) 165 V. See supplementary video clip 1 (3x slower).

When the bubble expands, the meniscus profile becomes convex out in the opening and the water in the channel is discharged. The discharge flow is pointed mainly in the axial direction of the channel. When the bubble shrinks, the meniscus is concaved into the microchannel so that water is drawn into the channel from all directions, as traced by the seeded particles. As a result, the particles along the channel axis have larger displacements in the expanding process than in the shrinking process while the particles near the rim of the channel opening is in the opposite case. As a result, the particles along the axis are expelled from the opening and the particles far off the axis are attracted to the opening during oscillation cycles. The arrows in Fig. 6 are added to describe the straight outgoing flow along the axis and two vortices on the sides of the channel opening. As time goes by, the generated flow sweeps the particles and creates a particle-empty region. The size of the empty region increases as the input voltage to the piezoelectric actuator increases (Figs. 6 (a-c)).

To see if this time-averaged (microstreaming) flow is strong enough to propel the device, a single bubble device is placed on the tank bottom after removing the anchor. If the generated propelling force is larger than the resistance caused by fluid drag and friction from the tank bottom, the device should be

able to be propelled. Fig. 7 (a) shows two snapshots of successful propulsion (also see the supplementary video clip 2, 60x slower). The device is propelled to the bottom-left corner. Here, a question is whether this propulsion is really generated by the streaming flow or other mechanisms. Apparently, there are other possible mechanisms for this propulsion: for example, (1) acoustic streaming between the interfaces of tank walls and water³⁴; and (2) asymmetric friction between the device and tank walls. In order to verify the truly responsible mechanism, the device is placed on a suspended glass plate in water that maintains a 2-mm gap above the tank bottom wall. Then, the direction of propulsion is checked for four initial orientations (0°, 90°, 180°, and 270°). For all the four initial orientations, the device is tested with the same input signal (11.2 kHz and 220 V_{pp}). Regardless of the initial orientation, the device is always propelled opposite to the opening side when the acoustic signal is applied. This means the streaming flow through the opening generates a pushing force since neither the acoustic streaming nor the asymmetric friction is closely correlated to where the opening is. As a result, it is concluded these two mechanisms are excluded from the responsible propulsion mechanism.

The device (5.4 mm \times 780 μm) with a channel array is also tested which has 10 microchannels parallel to each other and whose channel openings face in the same direction, as shown in Fig. 7 (b) (see the supplementary video clip 3, 16x slower). The input voltage is always fixed at 170 V_{pp} . When the driving frequency is also set at 11.2 kHz, the device shows best performance in propulsion. Fig. 7 (b) shows sequential snapshots of the motion at the speed of 3.87 mm/s. The propulsion direction is changed slightly due mainly to non-uniform friction between the device and the bottom of the testing tank. This array type device can be attached to any curved surface to propel large objects.

The rotation of the device could also be achieved by embedding bubbles on the turbo blades, as shown in Fig. 7 (c) (see supplementary video clip 4, 1.1x faster). There are six 820- μm channels on three turbo blades: two on each blade. The radius of the turbo device is 1750 μm and the device is anchored at the center by an optical fiber at the bottom of the testing tank. The channels are curved to fit in the blades. The signal is reduced to be 3.8 kHz (480 V_{pp}) due to the increased bubble length. The blades rotate continuously in the clockwise direction at 75 rpm. This rotational motion can be utilized and applied to drive micropumps, microvalves, micromixers, etc.

Carrying a payload is also examined. A testing load is made of a thin plastic film that is bent and glued to the two ends of the arrayed device as shown in Fig. 7 (d) (see supplementary video clip 5, 60x slower for translation and 25x slower for rotation). Because of the increased mass and surface area, friction from the tank bottom and drag are increased. It is difficult to get the similar propulsion using the previous voltage as Figs. 7 (a) and (b) (170 V_{pp}): A higher voltage of 190 V_{pp} is used. When the bubbles oscillate at 11.2 kHz, the device with the load is pushed away and rotated.

The effects of the input voltage and frequency on the propulsion speed are examined, as shown in Fig. 8. At 11.2

kHz, the propulsion speed increases as the voltage increases (Fig. 8 (a)). It is obvious that higher input voltages generate stronger acoustic fields. The acoustic pressure amplitudes measured by the miniature reference hydrophone are 3.16, 3.56 and 4.05 kPa for 170, 190 and 210 V_{pp} , respectively. The maximum velocity is even over 45 mm/s, about 50 body lengths per second. If the flap were removed, the velocity would be higher due to reduced friction and drag. The

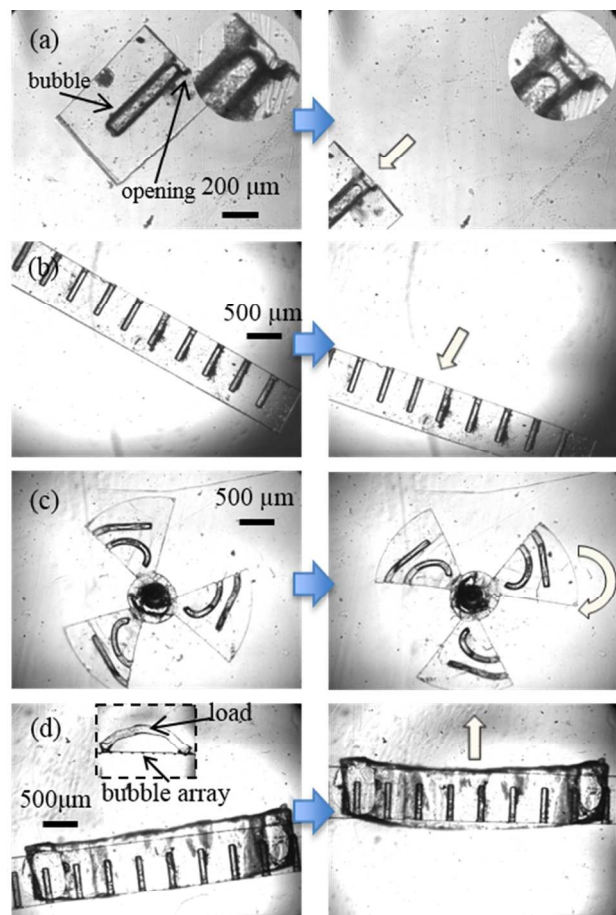


Fig. 7 (a) Propulsion by a single bubble (11.2 kHz, 170 V_{pp} ; see supplementary video clip 2, 60x slower; Insets show bubble menisci and channel opening), (b) Propulsion by an array of bubbles (11.2 kHz, 170 V_{pp} ; see supplementary video clip 3, 16x slower), (c) Rotation by bubbles embedded on turbo blades (3.8 kHz, 480 V_{pp} ; see supplementary video clip 4, 1.1x faster) and (d) Payload carrying by an array of bubbles (11.2 kHz, 190 V_{pp} ; see supplementary video 5, 60x slower for translation and 25x slower for rotation). The inset shows a side view of the arrayed bubbles and load. Note that due to aliasing of image sampling the bubble oscillations look slower than the applied frequency.

propulsion force F is estimated to be $\sim 0.8 \mu\text{N}$ by equation (2) When the input voltage is higher than 200 V_{pp} , the bubble oscillates so violently that the bubble trapped in the channel is broken into smaller bubbles. This results in reduction in the bubble size in the channel. Furthermore, the lifetime of the bubble would be much shorter and there would be a significant change in the resonant frequency.

Fig. 8 (b) shows the effect of the input frequency between 9 kHz and 12 kHz revealing a clear peak. For this frequency test, the voltage is fixed at 170 V_{pp} . The maximum propulsion speed

occurs at 11.2 kHz, which is about 7.5 mm/s. When the driving frequency is even slightly shifted, the propulsion speed decreases rapidly. In many cases, the motions are uncertain (stick-and-slip motions) due mainly to friction with the wall of the tank. It is possible to turn on and turn off this propulsion by simply changing the frequency of acoustic input. In addition, if multiple bubbles with different resonances are built on the same chip, changing the input frequency allows us to activate only selected bubbles. This can be used for 2-D propelling and steering³⁵.

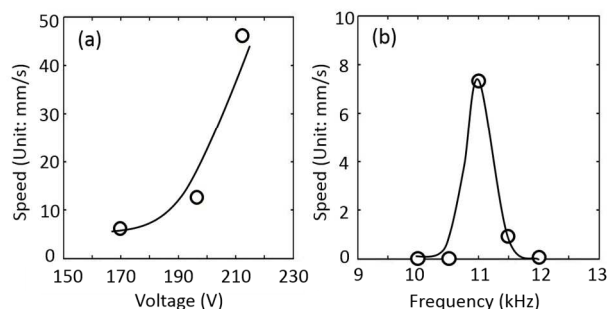


Fig. 8 Propulsion speed vs. (a) applied voltage and (b) frequency.

In both single bubble device and arrayed device, the maximum oscillation and propulsion speed occur at 11.2 kHz, which is slightly different from the frequency (10.5 kHz) predicted by equation (3). This difference can be explained by the effect of resonance behavior of the tank-water system. The oscillation spectrum of the tank bottom wall is measured by the LDV from 1 to 12 kHz with an interval of 1 kHz for three different water depths: 1 cm, 2 cm and 3 cm. The result indicates (not shown here) that the oscillating of water tank bottom has its own resonances and is strongly affected by the water depth. This is attributed to change in mass of the whole system when changing the water depth. When the water depth is 3 cm, which is set for all the experiments, there are two distinct peaks. The first peak occurs at 6 kHz and the second one does at 11 kHz. Since the acoustic waves oscillating the bubble are transferred mainly by bending waves in the tank walls, this spectrum will be very similar to the actual acoustic input to the bubble. That is the reason why the bubble oscillations are very strong at 6 and 11 kHz when the water level is set at 3 cm. In particular, the bubble oscillation is maximum at 11 kHz. Why does the maximum of bubble oscillation occur at 11 kHz, not 6 kHz? The answer is that the resonance frequency of the bubble (10.5 kHz, calculated by equation (3)) is very close to 11 kHz but far from 6 kHz. In order to predict the spectrum behavior of bubble oscillation (propulsion), all combined effects of the surrounding system need to be taken into account. In particular, the water level effect would be interesting for the future research. In addition, the loss (damping) mechanism^{19, 32} in oscillation is also important to relate the acoustic pressure input to the oscillation amplitude, which has not been studied here.

It was observed that the bubble size was reduced after oscillation (~20% after 1-hour oscillation). The main reasons for reduction are that the strong oscillation enhances the fluid mixing and thus gas dissolution and occasionally segregates the mother bubble into much smaller daughter bubbles. As a result, the resonance frequency was observed to shift.

Conclusions

This paper describes a micro propulsion method in water where a cylindrical gaseous bubble trapped in a microchannel and oscillated by an external acoustic excitation generates a microstreaming flow and a propelling force. Due to compressibility of the bubble, the bubble oscillates in the presence of an external acoustic field and periodically generates intake/discharge flows through the opening of the microchannel. 2-D computational fluid dynamics (CFD) simulations show that the difference between the intake and discharge flows increases and eventually generates a net flow (microstreaming flow), as the Reynolds number increases. This net flow in turn creates a propelling force against the microchannel device. Based on the simulations, a microchannel with one end section open is designed and fabricated from parylene using microphotolithography. The equivalent diameter of the microchannel is 60 μm , which is small enough to navigate narrow passages in microfluidic and *in vivo* environments. Upon submerging the channel in water, an air bubble is automatically trapped in the channel due to hydrophobic channel surfaces.

Although the device is in micro scale, the Reynolds number of the oscillatory flow can be maintained high enough to generate a net flow and thus strong propelling force. This is achieved by maximizing bubble oscillation and setting the frequency high (over 10 kHz). The frequency of the acoustic input is tuned to resonate the bubble. It turns out that for the best performance the frequency should match not only the resonance frequency of the system (including the water tank and water) but also the resonance frequency of the bubble itself, as evidenced by the oscillation spectrum of the testing setup measured by the LDV. When the frequency is well tuned, the generated force by a single bubble is strong enough to propel the device as fast as up to 45 mm/s, about 50 body lengths per second. In addition, it is shown that an array of bubbles can be simultaneously oscillated to propel a large device. When bubbles are embedded on the blades of micro turbo device, they generate a torque and rotate the device. In addition, the propelling device demonstrates payload carrying. Flow visualizations performed by tracing seeded microparticles confirm the microstreaming flow is generated by bubble oscillations, which is responsible for propulsion. Potential applications of this device may be mainly microswimmers that navigate microfluidic spaces as well as narrow passages inside human body to perform various missions such as bio sensing, drug delivery, and microsurgery.

Acknowledgements

This work was supported by the National Science Foundation under Grant (ECCS-1029318).

Notes and references

^a Department of Mechanical Engineering and Materials Science, University of Pittsburgh, Pittsburgh, PA 15261, USA (e-mail: jif17@pitt.edu).

^b Department of Mechanical Engineering and Materials Science, University of Pittsburgh, Pittsburgh, PA 15261, USA (e-mail: juy16@pitt.edu).

^c S. K. Cho (corresponding author) is an Associate Professor with Department of Mechanical Engineering and Materials Science, University of Pittsburgh, Pittsburgh, PA 15261, USA (e-mail: skcho@pitt.edu).

† Electronic Supplementary Information (ESI) available: 5 movie clips provided to enhance the understanding.

1. M. Sitti, Miniature devices: Voyage of the microrobots, *Nature*, 2009, **458**, 1121-1122.
2. S. Sengupta, M. E. Ibele and A. Sen, Fantastic voyage: Designing self-powered nanorobots, *Angew. Chem. Int. Ed.*, 2012, **51**, 8434-8445.
3. L. K. E. A. Abdelmohsen, F. Peng, Y. Tu and D. A. Wilson, Micro- and nano-motors for biomedical applications, *J. Mater. Chem. B*, 2014, **2**, 2395-2408.
4. J. Feng and S. K. Cho, Mini and micro propulsion for medical swimmers, *Micromachines*, 2014, **5**, 97-113.
5. L. Zhang, J. J. Abbott, D. Lixin, B. E. Kratochvil, D. Bell and B. J. Nelson, Artificial bacterial flagella: Fabrication and magnetic control, *Appl. Phys. Lett.*, 2009, **94**, 064107.
6. A. Ghosh and P. Fischer, Controlled propulsion of artificial magnetic nanostructured propellers, *Nano Lett.*, 2009, **9**, 2243-2245.
7. R. S. M. Rikken, R. J. M. Nolte, J. C. Maan, J. C. M. v. Hest, D. A. Wilson and P. C. M. Christianen, Manipulation of micro- and nanostructure motion with magnetic fields, *Soft Matter*, 2014, **10**, 1295-1308.
8. R. Dreyfus, J. Baudry, M. L. Roper, M. Fermigier, H. A. Stone and J. Bibette, Microscopic artificial swimmers, *Nature*, 2005, **437**, 862-865.
9. S. Martel, C. C. Tremblay, S. Ngakeng and G. Langlois, Controlled manipulation and actuation of micro-objects with magnetotactic bacteria, *Appl. Phys. Lett.*, 2006, **89**, 233904.
10. B. Behkam and M. Sitti, Bacterial flagella-based propulsion and on/off motion control of microscale objects, *Appl. Phys. Lett.*, 2007, **90**, 023902.
11. J. R. Howse, R. A. L. Jones, A. J. Ryan, T. Gough, R. Vafabakhsh and R. Golestanian, Self-motile colloidal particles: From directed propulsion to random walk, *Phys. Rev. Lett.*, 2007, **99**, 048102.
12. A. A. Solovev, Y. Mei, E. B. Ureña, G. Huang and O. G. Schmidt, Catalytic microtubular jet engines self-propelled by accumulated gas bubbles, *Small*, 2009, **5**, 1688-1692.
13. G. Zhao, M. Viehriig and M. Pumera, Challenges of the movement of catalytic micromotors in blood, *Lab Chip*, 2013, **13**, 1930-1936.
14. G. Zhao, H. Wang, B. Khezri, R. D. Webster and M. Pumera, Influence of real-world environments on the motion of catalytic bubble-propelled micromotors, *Lab Chip*, 2013, **13**, 2937-2941.
15. L. Soler, C. Martínez-Cisneros, A. Swiersy, S. Sánchez and O. G. Schmidt, Thermal activation of catalytic microjets in blood samples using microfluidic chips, *Lab Chip*, 2013, **13**, 4299-4303.
16. W. Gao, A. Uygun and J. Wang, Hydrogen-bubble-propelled zinc-based microrockets in strongly acidic media, *J. Am. Chem. Soc.*, 2012, **134**, 897-900.

17. L. Restrepo-Pérez, L. Soler, C. Martínez-Cisneros, S. Sánchez and O. G. Schmidt, Biofunctionalized self-propelled micromotors as an alternative on-chip concentrating system, *Lab Chip*, 2014, **14**, 2914-2917.
18. I. Finnie and R. L. Curl, Physics in a toy boat, *Am. J. Phys.*, 1963, **31**, 289-293.
19. R. J. Dijkink, v. d. D. Dennen, J.P., C. D. Ohl and A. Prosperetti, The “acoustic scallop”: A bubble-powered actuator, *J. Micromech. Microeng.*, 2006, **16**, 1653-1659.
20. K. Ryu, J. Zueger, S. K. Chung and S. K. Cho, Underwater propulsion using AC-electrowetting-actuated oscillating bubbles for swimming robots, presented in part at the Proceedings of 2010 IEEE 23rd International Conference on Micro Electro Mechanical Systems (MEMS), Wanchai, Hong Kong, 24-28 Jan. 2010, 160-163.
21. L. Qiao and C. Luo, Propulsion of a microsubmarine using a thermally oscillatory approach, *J. Micromech. Microeng.*, 2013, **23**, 105011.
22. A. Hashmi, G. Yu, M. Reilly-Collette, G. Heimana and J. Xu, Oscillating bubbles: a versatile tool for lab on a chip applications, *Lab Chip*, 2012, **12**, 4216-4227.
23. A. R. Tovar and A. P. Lee, Lateral cavity acoustic transducer, *Lab Chip*, 2009, **9**, 41-43.
24. K. Ryu, S. K. Chung and S. K. Cho, Micropumping by an acoustically excited oscillating bubble for automated implantable microfluidic devices, *J. Lab. Autom.*, 2010, **15**, 163-171.
25. S. K. Chung and S. K. Cho, On-chip manipulation of objects using mobile oscillating bubbles, *Journal of Micromechanics and Microengineering*, 2008, **18**, 125024.
26. S. K. Chung and S. K. Cho, 3-D Manipulation of millimeter- and micro-sized objects using an acoustically-excited oscillating bubble, *Microfluidics and Nanofluidics*, 2009, **6**, 261-265.
27. K. Ryu, S. K. Chung and S. K. Cho, Separation and collection of microparticles using oscillating bubbles, presented in part at the The 12th International Conference on Miniaturized Systems for Chemistry and Life Sciences (μ TAS 2008), San Diego, CA, October 12 – 16, 2008, 808-810.
28. M. V. Patel, I. A. Nanayakkara, M. G. Simona and A. P. Lee, Cavity-induced microstreaming for simultaneous on-chip pumping and size-based separation of cells and particles, *Lab Chip*, 2014, **14**, 3860-3872.
29. J. Feng and S. K. Cho, Micro propulsion in liquid by oscillating bubbles, presented in part at the Proceedings of 2013 IEEE 26th International Conference on Micro Electro Mechanical Systems (MEMS), Taipei, 20-24 Jan. 2013, 63-66.
30. A. Jenkins, Sprinkler head revisited: Momentum, forces, and flows in Machian propulsion, *Eur. J. Phys.*, 2011, **32**, 1213-1226.
31. E. M. Purcell, Life at low Reynolds number, *Am. J. Phys.*, 1977, **45**, 3-11.
32. X. M. Chen and A. Prosperetti, Thermal processes in the oscillations of gas bubbles in tubes, *J. Acoust. Soc. Am.*, 1998, **104**, 1389-1398.
33. T. Y. Chang, V. G. Yadav, S. D. Leo, A. Mohedas, B. Rajalingam, C.-L. Chen, S. Selvarasah, M. R. Dokmeci and A. Khademhosseini, Cell and protein compatibility of parylene-C surfaces, *Langmuir*, 2007, **23**, 11718-11725.
34. W. L. Nyborg, Acoustic streaming near a boundary, *J. Acoust. Soc. Am.*, 1958, **30**, 329-339.
35. J. Feng and S. K. Cho, Two-dimensionally steering microswimmer propelled by oscillating bubbles, presented in part at the Proceedings of 2014 IEEE 27th International Conference on Micro Electro Mechanical Systems (MEMS), San Francisco, CA, USA, 26-30 Jan. 2014, 188-191.